



TECHNICAL ARTICLE

Abrasive Wear Behavior of Fe-Based Amorphous/Nanocrystalline Coatings Deposited by High-Velocity Oxygen Fuel and Wire Arc Spray

Hipólito Carvajal Fals, Mario Sánchez Orozco, Luciano Augusto Lourençato, and Carlos Roberto Camello Lima

Submitted: 11 February 2022 / Accepted: 9 July 2022 / Published online: 6 September 2022

Abrasive wear behavior of high-pressure high-velocity oxygen fuel (HP-HVOF) and wire arc spray (WAS) iron-based coatings were compared. Microstructural analysis of the coatings was carried out by scanning electron microscopy and energy dispersive spectroscopy. X-ray diffraction was also used to characterize the microstructures of the coatings. A PANalytical X'Pert PRO diffractometer using a Cu-K α radiation source was utilized. The microhardness, porosity, and abrasive wear resistance of the produced coatings were compared. ASTM G65 standard was applied for the coatings' abrasive wear assessment using a dry sand rubber wheel abrasion test rig. The HVOF iron-based coatings showed amorphous structures, whereas the wire arc spray technique yielded polycrystalline coatings. The results show higher resistance to abrasive wear for the HVOF coatings in comparison with WAS coatings justified by the higher microhardness, higher amorphous fractions, and lower porosity induced by the process. The morphologies of the worn surfaces of both coatings demonstrated that a combination of micro-plowing and micro-cutting mechanisms has conducted the whole wear process.

Keywords abrasive wear, arc spray, Fe-based amorphous coatings, HVOF, thermal spray

1. Introduction

The abrasive wear performance of coatings depends on structural particularities such as dissimilarity of the composite structure, quantity of pores, and stress state of the surface. It also depends on mechanical properties such as hardness and toughness (Ref 1, 2). In laboratory conditions, hardness, shape, and size of the abrasive, wear velocity and angle of impact, and other experimental conditions such as temperature and testing media must also be taken into account (Ref 3).

Wear resistance at different abrasive wear conditions of traditional tungsten carbide-cobalt (WC-Co) based coatings have been extensively studied because this material group is widely used in several industries. However, the demand for iron-based coatings has increased due to industrial applications requiring high wear resistance at elevated temperatures such as gas turbines, boilers, and hydraulic turbine blades (Ref 4, 5). Iron (Fe)-based composite amorphous coatings have an interesting combination of properties like high hardness, high strength, improved wear, and corrosion resistance, turning them

into a class of important engineering materials for coatings (Ref 6-8).

Thermal spray technologies, such as Wire Arc Spray (WAS) and high-velocity oxygen fuel (HVOF), among other processes, are supposed to produce amorphous Fe-based composite coatings promoting extended surface protection. In general, thermal spray processes have high efficiency, and friendly operation, and allow a wide range of different materials, being accepted in numerous industries. Several investigations on the mechanical properties, microstructural characteristics, and wear behavior of Fe-based amorphous hard coatings deposited by thermal spray processes have been reported (Ref 5, 9-13).

Cheng et al. (Ref 5) have used arc spraying to produce amorphous FeBSiNb coatings applied to improve the erosion resistance in boilers working at elevated temperatures. The authors also evaluated in detail the correlation between coating microstructure and erosion resistance. They found moderate degradation of the coating at lower impact velocity and lower impact angles, contrasting with severe damage for higher velocities and higher impact angles. Then, they concluded that FeBSiNb coating showed outstanding erosion resistance at high temperatures at least up to 600 °C in service.

Lin et al. (Ref 9) prepared three different Fe-based coatings using the process of twin wire arc spraying, investigating the microstructure and corrosion behavior of the coatings. The results showed that the FeNiCrBSiNbW coating presented much higher corrosion resistance as compared with FeB and FeBSi coatings. This result was credited to the amorphous/nanocrystalline structure as well as to the presence of Cr in the alloy improving the corrosion resistance.

Liu et al. (Ref 10) have tested HVOF Fe-based alloy coatings deposited on stainless steel. The feedstock alloy was modified by adding cobalt. Following spraying, coatings were heat-treated at 500 to 900 °C for up to three hours in a vacuum

Hipólito Carvajal Fals and **Luciano Augusto Lourençato**, Universidade Tecnológica Federal do Paraná, Ponta Grossa, Paraná, Brazil; **Mario Sánchez Orozco**, Universidad de Oriente, Santiago, Cuba; and **Carlos Roberto Camello Lima**, Mackenzie Presbyterian University, Rua da Consolação, São Paulo, Brazil. Contact e-mails: ccamellolima@gmail.com and carlos.lima@mackenzie.br.

furnace. From the microstructures and phases analysis, the authors found that adding a cobalt material to Fe-based alloy yields coatings with enhanced corrosion and tribological characteristics.”

Gu et al. (Ref 11) prepared Fe-based coatings with a high glass-formation ability using twin wires arc spray technology. They applied a rapid arc spray melting and solidification process. Then, crystalline phases were not identified from the XRD patterns, showing coatings comprised of fully amorphous phases, with a dense structure and a low porosity of only 2%. The amorphous Fe-based coatings exhibited high hardness (900–1100 HV0.3) and superior bonding strength (44.9–54.8 MPa).

Guo et al. (Ref 12) deposited Fe-Cr-Nb-B by HVOF spraying producing amorphous/nanocrystalline coatings. The substrate was 410 stainless steel. Inside the amorphous phase, nanocrystals of α -Fe, FeB, and Fe₂B were also detected. The coating revealed higher microhardness and wear resistance compared to the steel substrate justified by the presence of Nb-rich borides, like (Fe, Cr)NbB, built in the amorphous matrix.

In 2017, Cheng et al. (Ref 13) studied the impacts of Cr and Nb additions on the mechanical properties and microstructure of FePSiB coatings applied by wire arc spraying. The authors widely discussed the connections between the glass-formation ability (GFA), the precipitated primary phase, and the mechanical properties of the coatings.

In the same year, Zhou et al. (Ref 14), using a supersonic plasma spraying, examined the influence of the Ar flow rate and process power on the microstructures and content of the amorphous phase of Fe₄₈Cr₁₅Mo₁₄C₁₅B₆Y₂ coatings. They also assessed the tribological behavior of the coatings using a sliding tribometer in the pin-on-disk mode. They found that increasing the Ar flow rate initially increases the microhardness and the content of the amorphous phase and further gradually decreases. After 30 min of testing and applying a load of 20 N, the coatings present similar steady-state coefficients of friction (0.75–0.82).

Recently, Koga et al. (Ref 15) have sprayed amorphous coatings through high-velocity oxygen fuel (HVOF) and flame spraying. They compared the hardness, thermal, and corrosion behavior of the produced coatings. From the electrochemical measurements, HVOF coatings showed higher corrosion resistance than the coatings applied by flame spray.

The literature reviewed for this study is centered on mechanical properties, corrosion, and erosion wear of thermally sprayed coatings. However, not much information is available on the abrasive wear behavior of amorphous iron-based coatings deposited by HVOF and Wire Arc Spraying. This paper aims at investigating the microstructure, porosity, microhardness, and abrasive wear resistance of HVOF and WAS iron-based amorphous coatings.

2. Materials and Methods

For the development of this investigation, two different coatings were produced by employing a twin wires arc spray system (AS 8830—Praxair TAF A), and a High-Pressure High-Velocity Oxi-fuel (HP-HVOF) using a JP-5000 (Praxair TAF A) Hypersonic torch. AISI 1020 low carbon steel 25 mm × 75 mm and 12 mm thick, was used as substrate. The parameters of the HVOF and WAS processes are shown in Table 1. They

were selected based on the manufacturer’s recommendations and also on preliminary tests carried out aiming at obtaining homogeneous layers with good adhesion in both processes.

The substrate surfaces were machined and gritblasted with aluminum oxide particles immediately before spraying, increasing the contact area and removing impurities. The resulting surface roughness for samples to be coated by both WAS and HVOF techniques was Ra 6 μ m, to guarantee a correct adhesion of the layer and to eliminate dirt and oxides. The surfaces were also cleaned with the ultrasound technique and then acetone was applied to remove moisture.

Iron-based material was used as feedstock material. A commercial powder Weartech SHS@9172HV (Lincoln Electric) – 53 + 15 μ m particle size was used for HVOF spraying. Twin wires of Lincoln SHS® 9172 W (Lincoln Electric) 1.6 mm diameter were applied to produce the WAS coatings. Table 2 shows the chemical composition of the feedstock materials given by the manufacturer.

The microstructural analysis of the coatings was performed by scanning electron microscopy using an EVOMA 15—Carl Zeiss coupled to energy dispersive spectroscopy (EDS). The EDS technique identified the chemical composition at specific points in the microstructure of the HVOF and WAS coatings. X-ray diffraction (XRD) was used to analyze the microstructure of the coatings using a PANalytical X’Pert PRO diffractometer and applying a Cu-K α radiation source. XRD scans were performed with a scan range of 20–80° (2 θ), with a step size of 0.01° and scan type continuous.

Porosity was determined using image analysis software (ImageJ 1.4 8v) from SEM magnified (500X) images of the cross section of the coatings. Pore area percentages were calculated from total pore area versus total coating area, according to ASTM method E2109-01. Three SEM images of each coating were used, and these SEM images were divided into ten areas, and the mean porosity values (total pore area versus total coating area %) were calculated and reported along with the standard deviation. Considering the limitations of the image analysis technique, in the correct detection of porosity, micrographs obtained by the backscattered electron technique were used, with a magnification of 500X, to ensure good characterization and good contrast between the phases, matrix, oxides, and porosity. A detailed analysis was also performed, and the best image thresholding techniques were selected to correctly define the gray levels, to improve the porosity estimation.

The microhardness measurements (HV_{0.5}) of the coatings were obtained by Vickers indentation, a load of 500 g, and residence time of 15 s using a Shimadzu HMV 2 T device. The load of 500 g allows obtaining an adequate size of the indentation, ensuring correct diagonal measurement. A total of 30 indentations were performed along the cross section of each coating, forming a 50 × 50 μ m matrix, 20 μ m away from the surface and 50 μ m from the substrate interface.

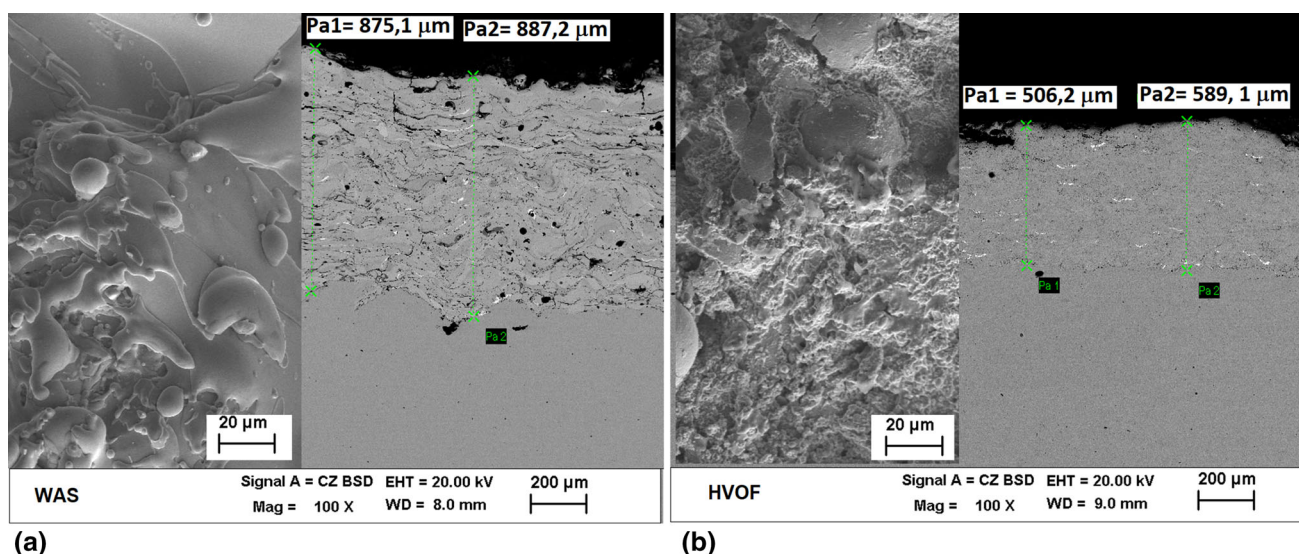
The dry sand rubber wheel abrasion test bench was applied to evaluate the abrasive wear behavior of linings according to procedure B of the ASTM G65 standard. Five samples of each coating thickness (25 × 75 × 12.5 mm) were used. Dry quartz sand AFS 60/70 was used as the abrasive in this test. The abrasive was not recycled during the tests which were carried out dry. The test sample was pressed with a 130 N load against the wheel at 2000 rpm. At the same time, sand was introduced as an abrasion agent at a flow rate of 400 g/min. Assays were stopped every 1 min of testing, which is equivalent to 1436 m,

Table 1 Main parameters used for thermal spraying of the feedstock material

WAS process				
Standoff distance, mm	Air pressure, Bar	Spraying voltage, V	Spraying current, A	
130	5,5	34	200	
HVOF process				
Standoff distance, mm	Oxygen, scfh	Nitrogen, scfh	Kerosene, GLP	Rotation speed of the powder feeder, RPM
350	2000	23	6	350

Table 2 Chemical composition of the feedstock materials

Thermal spray	Material form	Chemical composition, %Wt.								
		Cr	W	B	Mo	Nb	C	Mn	Si	Fe
WAS	Twin wires	<25	<15	<5	<6	<12	<4	<3	<2	Balance
HVOF	Powder	<25	<5	<5	<6	<12	<4	<3	<2	Balance

**Fig. 1 SEM images of the as sprayed coatings (100X): (a) WAS coating, (b) HVOF coating**

to control mass loss. The total duration of the tests was 5 min, accumulating a total of 7160 m of abrasive surface examined.

Ultrasonic cleaning in acetone was conducted for the samples before and after tests. The results of mass loss (W_g) were taken by direct weighing on a precision scale (0.001 g). Volume losses (W_v) were determined using Eq 1, as explained in the ASTM G65 standard. Density values (ρ) of 7.59 g/cm³ for the HVOF deposited coatings and 7.68 g/cm³ for the arc spray deposited coatings were used.

$$W_v = \frac{W_g(g)}{\rho\left(\frac{g}{cm^3}\right)} \cdot 1000 (mm^3) \quad (\text{Eq 1})$$

3. Results and Discussion

3.1 Microstructural Characterization

SEM image micrographs of the transverse section and the surface of the WAS and HVOF coatings are, respectively,

presented in Fig. 1. The coatings presented different microstructures depending on the process used, namely WAS or HVOF. The coatings obtained by the WAS process showed greater microstructural heterogeneity, with the formation of splats shaped lamellae of molten and partially molten particles, as can be seen in Fig. 1(a). It is also observed the formation of interlayer oxides, in addition to pores and voids. Occasionally, unmelted particles can be seen in the microstructure of the coatings and appear to be larger, or probably these particles were projected by cooler marginal areas of the flame, making the melting process difficult. Typically, unfused particles within a coating microstructure are undesirable and should be minimized. HVOF coatings were denser (Fig. 1b); however, some porosity or inter-splat voids are observed that can affect the cohesion between the splats.

The average thicknesses of the coatings were measured from the images of the cross sections, carried out in SEM. Five measurements were performed for each coating. Figure 1(A) shows that the coatings obtained by WAS showed an average thickness of $880 \pm 47 \mu\text{m}$ greater than the average value

obtained by the HVOF process ($530 \pm 57 \mu\text{m}$), shown in Fig. 1(B).

Figure 2 illustrates the processing sequence of SEM images of the cross sections of the coatings, illustrating how porosity was achieved. From the SEM images (Fig. 2a and c) eight-bit images in black-and-white are produced (Fig. 2b and d) using the image processing software, separating the pores, and allowing further analysis and counting. The SEM images were divided into ten areas, as described above, and the average porosity values (%) were determined.

Figure 2 also corroborates that the HVOF coating (Fig. 2c) has a dense structure with a very fine microstructure, with the presence of carbide grains and low porosity ($0.25 \pm 0.03\%$). The lamellar structure, resulting from the continuing accumulation of molten or unmolten particles on the substrate, and pores in the inter-splats areas (dark areas) are visible in the WAS coatings (Fig. 2a). These coatings have average porosity values of $1.87 \pm 0.56\%$ in the samples analyzed, similar to the value obtained by Lin et al. (Ref 9), in Fe-based coatings (FeNiCrBSiNbW).

EDS analysis of the coatings applied by the HVOF process is presented in Fig. 3. Spectrum 1 (Fig. 3a) located in a carbide shows a greater presence of W, in addition to Fe. Spectrum 2 (Fig. 3b) shows the presence of the main coating components: Fe, Cr, Si, Nb, and Mo. Figures 3(a) and (b) also illustrate the region where the analysis was performed (upper right corner).

3.2 XRD Analysis of the Coatings

The XRD patterns of the WAS and HVOF coatings are displayed in Fig. 4. The XRD patterns were compared with several diffractograms of the Powder Diffraction File (PDF®) database. In the diffraction spectrum of the HVOF coating, shown in Fig. 4, it can be noted that there is a predominant wide deformation in the spectrum background (2θ of 45°), typical of amorphous metallic glass matrix composite, as already was proved by Lin et al. (Ref 9).

Coatings with similar microstructural formation were found by Zhou et al. (Ref 16). The authors verified that the wide deformation in the x-ray diffraction spectrum of this type of HVOF coating specified the significant volume fraction of the glass matrix; they have also detected similar results in the small volume fractions of crystalline phases further identified as α -Fe (ferrite) and $M_2(BC)$, M referring to a blend of transition metals. The diffraction concentrations of all other crystalline peaks are much lower than the amorphous hump.

When the cooling rates are high enough to hinder the crystallization kinetics, amorphous structures commonly are formed. Sudden temperature drops in the HVOF technique could indicate the probability of amorphous structure formation in coatings. Undoubtedly, the high-velocity oxy-fuel spraying is of special benefit in this regard, allowing individual molten droplets to be cooled at a rate of up to 10^5 K/s, which facilitates amorphous phase formation (Ref 17, 18)

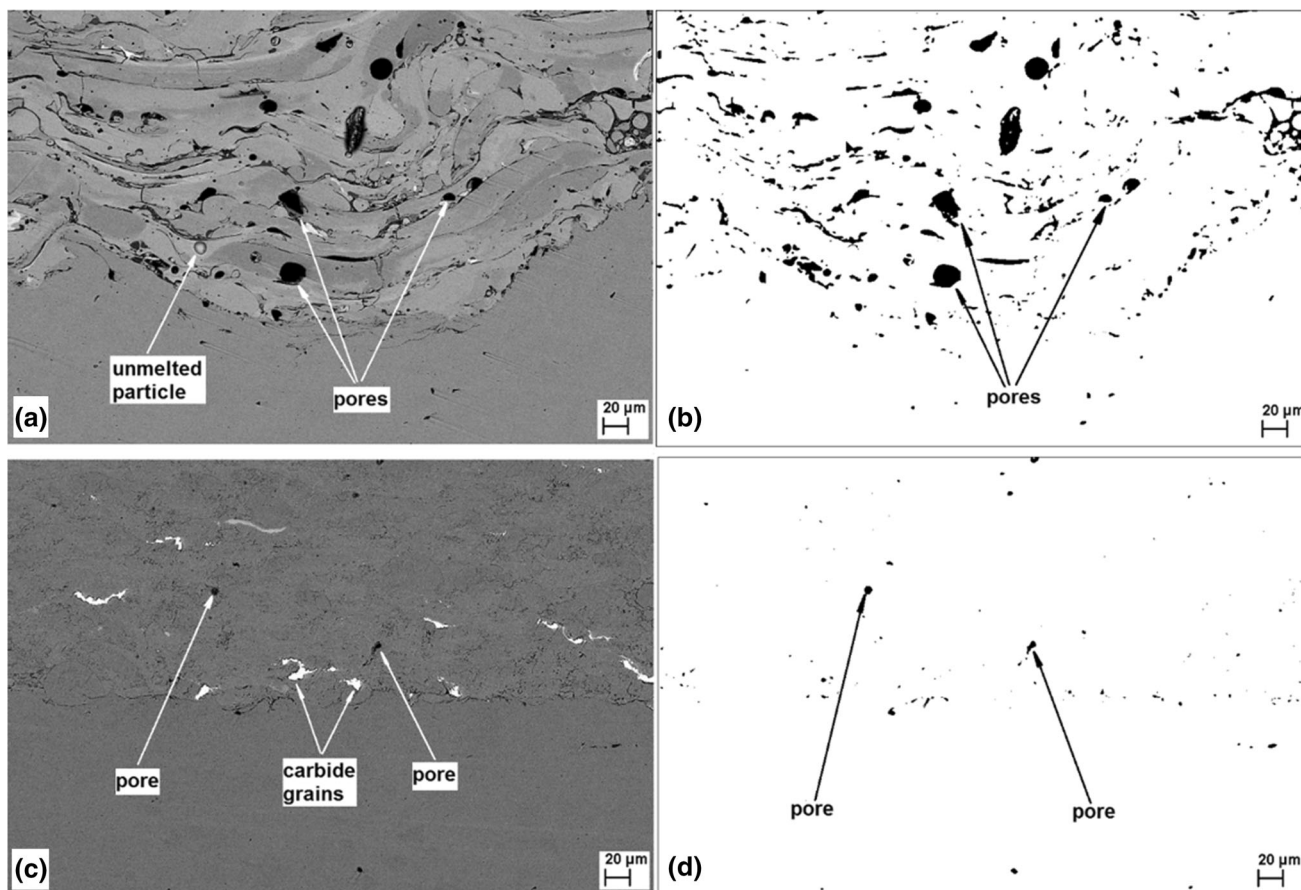


Fig. 2 Processing Sequence of SEM images of the coatings. (a) WAS coating cross section of (500X), (b) Cross section of WAS coating (8 bits image); (c) Cross section of HVOF coating (500X); (d) Cross section of HVOF coating (8 bits image)

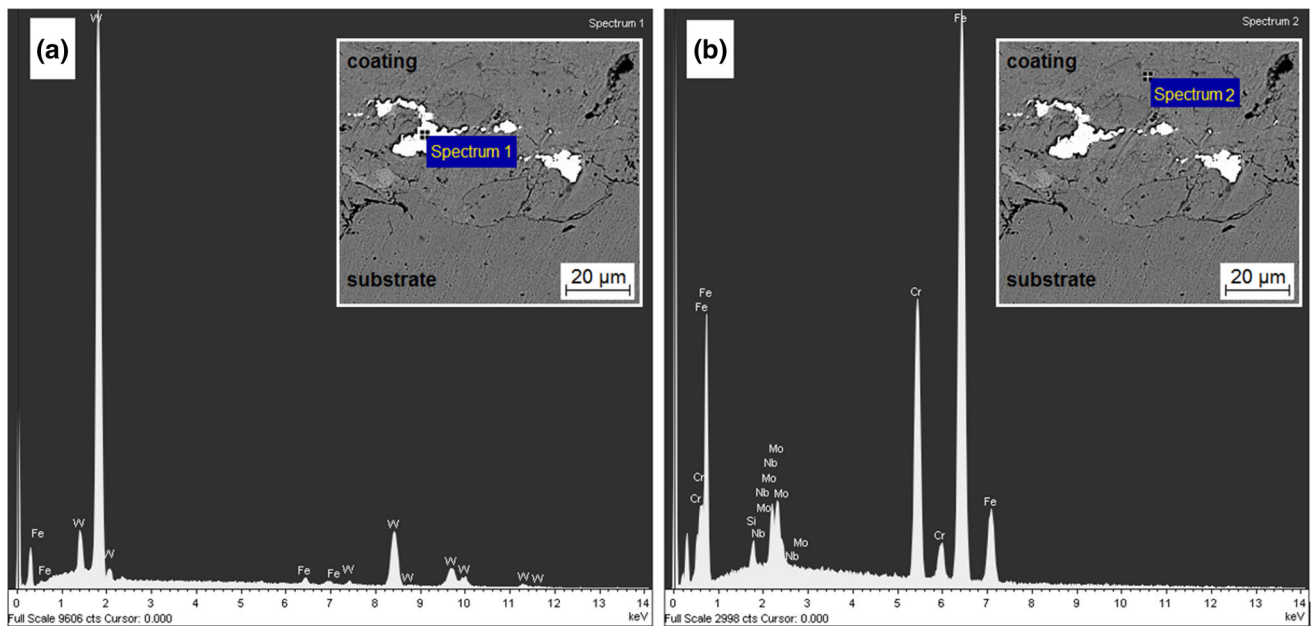


Fig. 3 EDS spectroscopy of the HVOF coating. (a) Spectrum 1 and (b) Spectrum 2

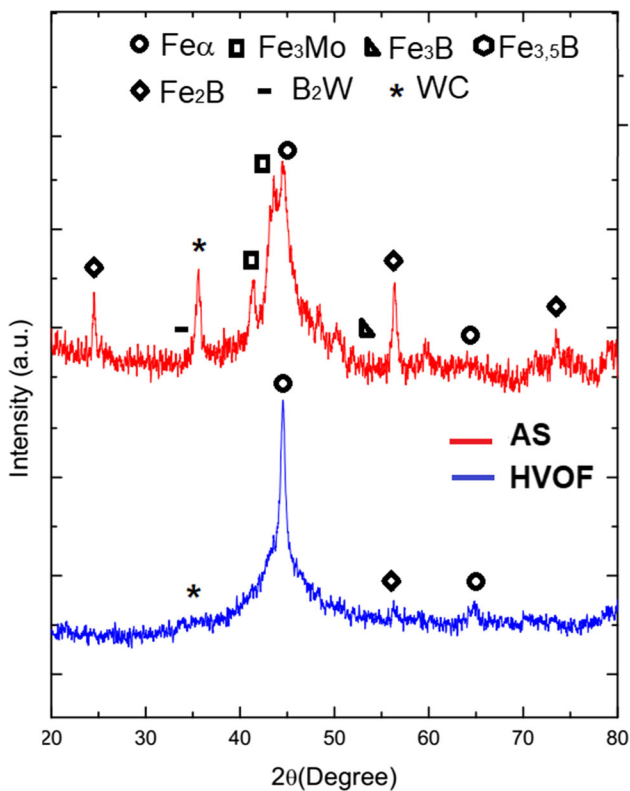


Fig. 4 XRD patterns of the Fe-based coatings

On the other hand, the formation of these Fe-based coatings by the electric arc process (WAS) with higher heat input, resulted in the formation of bimodal amorphous microstructure with various nanocrystalline phases (Fe_2B , $\text{Fe}_{3.5}\text{B}$, Fe_3B , Fe_3Mo , B_2W , and WC) as shown in XRD pattern in Fig. 4. This observation is according to Kumar et al. (Ref 19), who also observed a higher fraction of nanocrystals when the power of the plasma spray process (APS) increased.

It can be said that the crystallinity of this amorphous coating, regardless of the chemical composition that characterizes the glass-forming ability (GFA), is influenced by several factors and parameters that define the formation and solidification of coatings in the WAS process (Ref 6). The Fe-based coatings obtained by the WAS process formed with higher heat input and successive deposition mechanisms of larger and different-sized fused splats, which release latent heat during solidification. Still, in the solidification of the splats, there are places with compositional inhomogeneities that can become the driving force of the transformation and promote nucleation.

Furthermore, the molten droplets driven by the carrier gas are oxidized over a greater surface area, due to the longer time at high temperatures. These oxides can act as sites for heterogeneous nucleation and the partial oxidation of particles results in a decrease in the content of metallic elements in the coating, which reduces the amorphous content (Ref 21).

Therefore, the slower cooling of the splats in the WAS technique and the formation of oxides result in easy crystallization and the formation of nanocrystalline coatings inside an amorphous matrix, as seen in Fig. 4.

As analyzed by Zhang et al. (Ref 20), in Fe-based coatings, the amount of amorphous phase initially depends on the quality of the particle melt during the spraying process. In this sense, incomplete fusion of some of the particles was observed more frequently in the WAS process. Also, in the unfused zones, the amorphous phase crystallizes under the influence of the thermal regime imposed by the fused zones.

Finally, it can be confirmed that the microstructure determined in the XRD analysis indicates that the coatings obtained by HVOF formed amorphous structures with very tiny crystallization because of the fast-cooling rates. However, the coatings obtained by WAS formed a bimodal nanocrystalline structure, as was also confirmed by Varadaraajan et al. (Ref 17).

3.3 Hardness Measurements

Microhardness was assessed along the coatings cross section, separating 50 μm between indentations. The profiles of the

median values of microhardness of both coatings are observed in Fig. 5. It was verified that the microhardness profiles show variability in the cross section of both coatings, but the coatings deposited by arc spray show greater variation, associated with lamellar formation, oxides and interlamellar pores, and greater porosity (7.5 times higher than HVOF coatings).

The coatings applied by HVOF showed an average microhardness value of $1344 \pm 125 \text{ HV}_{0.05}$. The average microhardness value of the WAS coatings was $1210 \pm 132 \text{ HV}_{0.05}$, with results similar to those obtained by Liu (Ref 6). The average microhardness values of the HVOF coatings can be considered 11% higher than those obtained for the WAS coatings, despite the high standard deviation values of the microhardness values reported here, which may represent a lack of statistical confirmation, meaning equal average values. In this sense, it is important to explain that the high deviations of microhardness measurements are characteristic of these types of coatings and are a consequence of the high macro (splats formation, pores, and interlamellar oxides) and microstructural heterogeneity. Therefore, the results allow us to confirm that the coatings with higher amorphous and dense fractions (HVOF), understood in this case as low porosity, generally presented higher average microhardness.

In the coating obtained by the WAS process in Fig. 5(a) there was a reduction in hardness at a depth of about $100 \mu\text{m}$ below the surface. This may be associated with the edge effect, with a higher concentration of defects in the region, mainly interlamellar microcracks (Fig. 1), caused by tensile thermal stresses that occurred in the final cooling stage of the coating.

Therefore, the results allow us to confirm that the coatings with higher amorphous and dense fractions (HVOF), understood in this case as low porosity, generally presented higher average microhardness.

3.4 Abrasive Wear Behavior

The volume loss of the coatings after the abrasive wear tests is shown in Fig. 6, which also shows details of the morphology of the worn surface of the coatings. It is observed that the HVOF coatings have a lower volume loss ($4.95 \pm 0.4 \text{ mm}^3$), compared to the WAS coatings, which were $12.76 \pm 1.14 \text{ mm}^3$. Five samples were tested for each condition. The greater homogeneity, less porosity, and greater hardness of the HVOF coatings meant a

less volumetric loss of material and a smaller standard deviation of wear values and, therefore, greater resistance to abrasive wear, which can also be attributed to their higher amorphous fractions, which were formed during the deposition process (Ref 22).

The higher abrasive wear resistance of the HVOF-deposited coating did not depend solely on its denser structure, but also on its higher amorphous phase content. Amorphous phases, as explained by Zhou et al. (Ref 14), due to the absence of grain boundaries and dislocations, have beneficial combinations of high strength, high elastic limits, and excellent wear resistance.

On the other hand, there is a direct relationship between hardness and wear rate in amorphous Fe-based coatings. According to Guo et al. (Ref 6), it can be concluded that the wear resistance properties of coatings are strongly affected by hardness, as observed.

In the analysis of abrasive wear of coatings deposited by the WAS process, it is important to understand that in addition to hardness there is a demonstrated correlation between wear and the relationship between hardness and Young's modulus (H/E). In this sense, it is reported by Yang et al. (Ref 22), that Young's modulus (E) in these materials can be improved by precipitating a greater fraction of nanocrystalline (Fe_2B and Fe_3B) in the amorphous matrix of the coating, which results in a lower H/E value. This may also be an explanation for the higher abrasive wear losses of the WAS coating with a lower amorphous fraction.

Studying the wear processes, the surfaces of the coatings were further observed by SEM at different magnifications after the abrasive wear test, as shown in Fig. 6. In the microscale image (Fig. 6, right), microcracks caused by cyclic shear stress can be observed on the worn surface of the WAS coating. Also, furrows produced during the test are noticeable, provoked by the repeated action of the abrasive particles. From deep and careful observation, the worn surface also shows pores and partially melted particles. The mean wear mechanism was micro-plowing and micro-cutting of the coating surface.

In the HVOF sample, the worn surface appears shallow, and furrows are less numerous compared to WAS coatings, which is consistent with the higher microhardness and lower wear rate of this sample. In some areas, abrasive particles work together with the edges of pores, causing material removal.

As can be seen, the whole material was worn out and the surface roughness of both coatings became smooth. Both

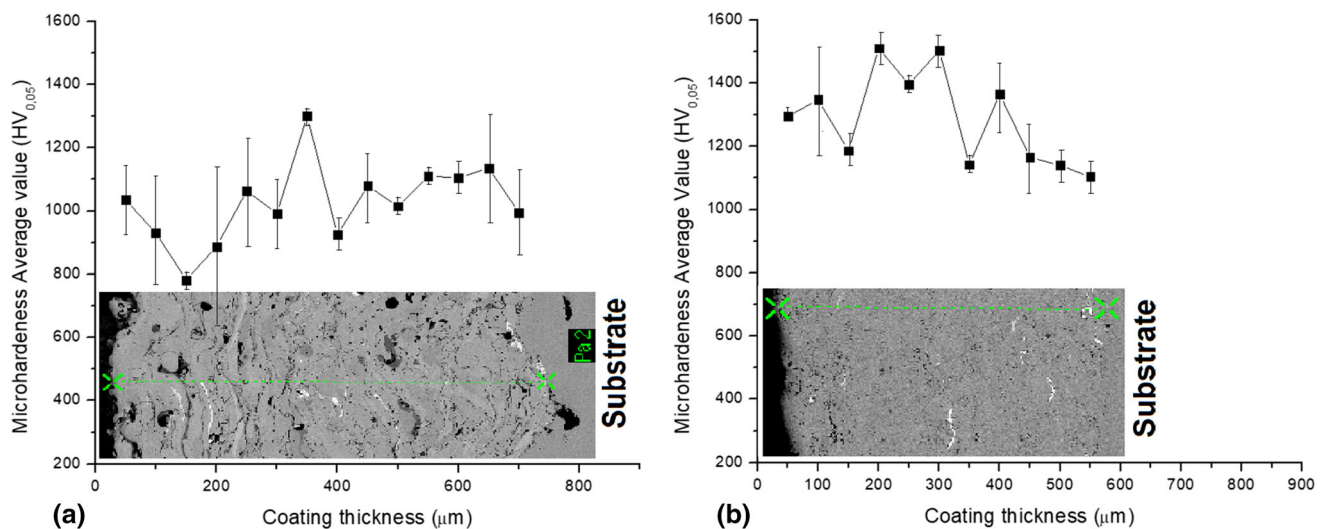


Fig. 5 Microhardness profile in the coatings cross section. (a) WAS coating. (b) HVOF coating

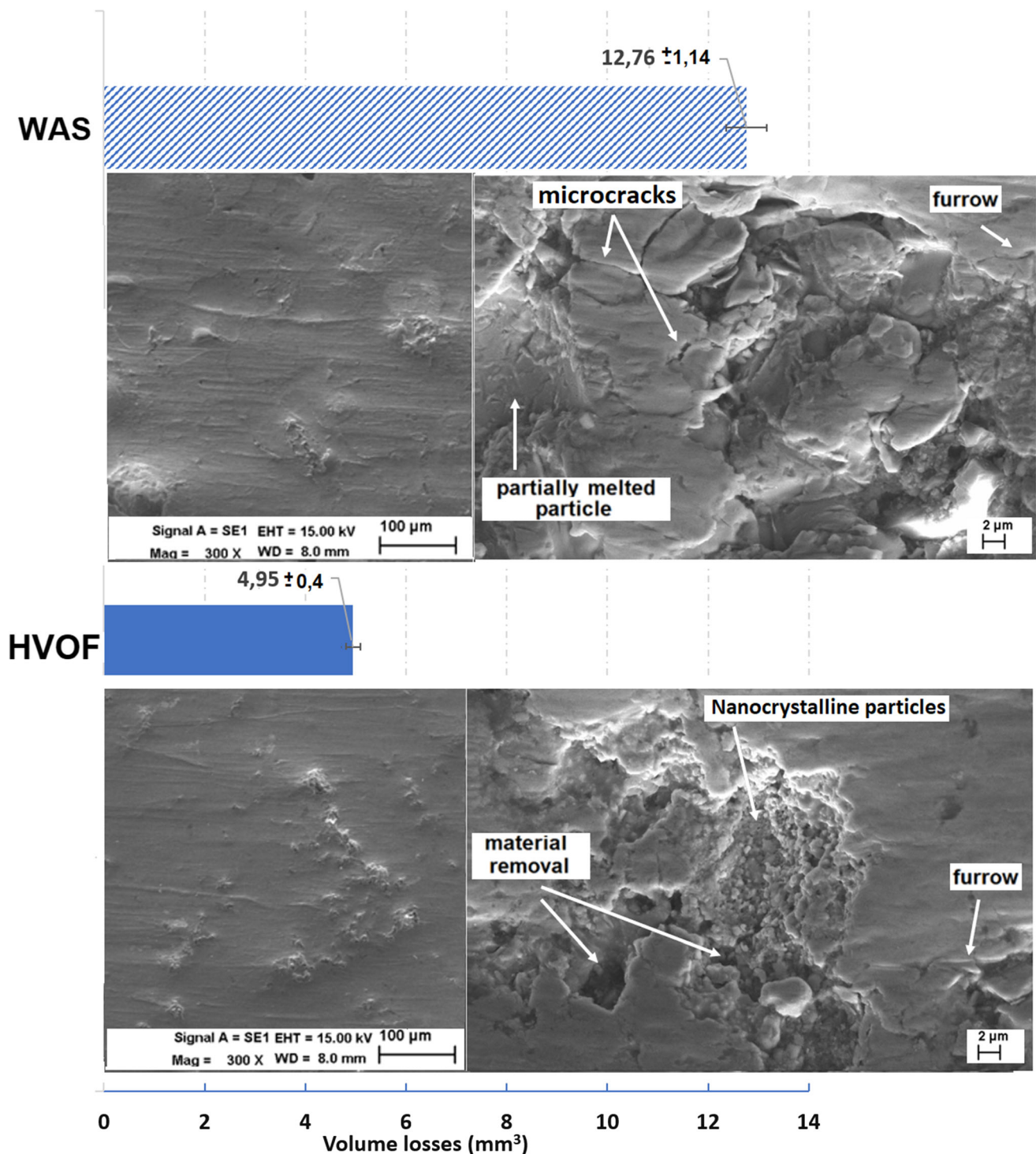


Fig. 6 Abrasive volume loss data for WAS and HVOF coatings. The SEM images of the worn surfaces are shown in lower (left) and higher magnification (right)

HVOF and WAS coatings presented a similar wear mechanism, i.e., plowing and cutting of coating surface. From the previous analysis, the high wear resistance of HVOF coating is determined not only by its higher amorphous fractions and homogeneous dense structure but also by its enhanced hardness and lower porosity. The worn surface of the HVOF coating has a shallower depth track than WAS coating, which evidences the higher abrasive wear resistance of HVOF coatings.

4. Conclusions

From the obtained results, it is possible to understand the abrasive wear behavior of the iron-based coatings applied on carbon steel substrate (AISI 1020) utilizing the wire arc spray and high-velocity oxygen fuel process:

- Fe-based HVOF coatings with a lower thickness ($530 \pm 57 \mu\text{m}$) and denser compared to coatings applied

by the WAS process ($880 \pm 47 \mu\text{m}$) were obtained. The porosity of WAS coatings was 7.5 times higher compared to HVOF coatings.

- XRD analyzes indicated that the deposition of the coatings with the HVOF technique allowed the formation of amorphous structures with slight crystallization, mainly due to the higher cooling rates, the chemical composition, and the type of raw material of the Fe-based coatings. On the other hand, the use of the WAS technique favored the formation of mainly crystalline coatings, influenced by the formation of the layer, with sequences of larger splats that reduced the cooling rate and also the formation of oxides, which favored the formation of nuclei of solidification.
- HVOF coatings showed high average microhardness values, 11% higher than those obtained for WAS coatings. The average microhardness value of the HVOF coatings was $1344 \pm 195 \text{HV}_{0.5}$ and for the WAS coatings, it was $1210 \pm 171 \text{HV}_{0.5}$. The results show that the coatings with lower porosity and higher amorphous fractions (HVOF) showed higher microhardness.
- The Fe-based coatings obtained by the HVOF process showed greater resistance to abrasive wear, showing lower volumetric losses (2.5 times less), compared to the coatings manufactured by the WAS technique. The abrasive wear mechanism was characterized by a combination of micro-plowing and micro-cutting phenomena.
- Comparing the HVOF and WAS spray processes, in the application of Fe-based coatings, it can be stated that the use of the HVOF technique favors the formation of Fe-based coatings with greater hardness and resistance to abrasive wear, based on the formation of a denser layer mostly amorphous and low crystallinity.
- Finally, considering the high flexibility and low cost of the WAS process, in-depth studies are required on the optimization of the process parameters to reduce the size of the splats and the formation of oxides in the coating, which enables the formation of a higher percentage of amorphous phases to achieve high abrasive wear resistance.

Acknowledgment

Carlos Lima and Hipólito Fals thank the technical support of OPT Brasil in the deposition of the coatings.

References

1. Y. Liu, T.E. Fischer, and A. Dent, Comparison of HVOF and Plasma-Sprayed Alumina/Titania Coatings—Microstructure, Mechanical Properties and Abrasion Behavior, *Surf. Coat. Technol.*, 2003, **167**(1), p 68–76. [https://doi.org/10.1016/S0257-8972\(02\)00890-3](https://doi.org/10.1016/S0257-8972(02)00890-3)
2. H. Liao, B. Normand, and C. Coddet, Influence of Coating Microstructure on the Abrasive Wear Resistance of WC/Co Cermet Coatings, *Surf. Coat. Technol.*, 2000, **124**(2), p 235–242. [https://doi.org/10.1016/S0257-8972\(99\)00653](https://doi.org/10.1016/S0257-8972(99)00653)
3. P. Kulu, R. Tarbe, and A. Vallikivi, Abrasive Wear of Powder Materials and Coatings, *Mater. Sci.*, 2005, **11**(3), p 230–234.
4. B. Wielage et al., Iron-Based Coatings Arc-Sprayed with Cored Wires for Applications at Elevated Temperatures, *Surf. Coat. Technol.*, 2013, **220**(1), p 27–35. <https://doi.org/10.1016/j.surfcoat.2012.12.013>
5. J. Cheng et al., High-Temperature Erosion Resistance of FeBSiNb Amorphous Coatings Deposited by Arc Spraying for Boiler Applications, *J. Therm. Spray Technol.*, 2013, **22**(5), p 820–827. <https://doi.org/10.1007/s11666-012-9876-5>
6. W. Guo et al., Fabrication and Characterization of Thermal-Sprayed Fe-Based Amorphous/Nanocrystalline Composite Coatings: An Overview, *J. Therm. Spray Technol.*, 2014, **23**(7), p 1157–1180. <https://doi.org/10.1007/s11666-014-0096-z>
7. H.R. Ma et al., Fe-Based Amorphous Coating with High Corrosion and Wear Resistance, *Surf. Eng.*, 2017, **33**(1), p 56–62. <https://doi.org/10.1080/02670844.2016.1176718>
8. C. Li et al., Effects of Heat Treatment on HVOF-Sprayed Fe-Based Amorphous Coating, *Surf. Eng.*, 2021, **37**(5), p 590–598. <https://doi.org/10.1080/02670844.2020.1759936>
9. J. Lin et al., Microstructure and Corrosion Resistance of Fe-Based Coatings Prepared by Twin Wires Arc Spraying Process, *J. Therm. Spray Technol.*, 2014, **23**(3), p 333–339. <https://doi.org/10.1007/s11666-013-0017-6>
10. W.H. Liu, F.S. Shieu, and W.T. Hsiao, Enhancement of Wear and Corrosion Resistance of Iron-Based Hard Coatings Deposited by High-Velocity Oxygen Fuel (HVOF) Thermal Spraying, *Surf. Coat. Technol.*, 2014, **249**(1), p 24–41. <https://doi.org/10.1016/j.surfcoat.2014.03.041>
11. W. Guo et al., Fabrication and Characterization of Fe-Based Amorphous Coatings Prepared by High-Velocity Arc Spraying, *Mater. Design*, 2015, **78**(1), p 118–124. <https://doi.org/10.1016/j.matdes.2015.04.027>
12. Y. Guo, G.Y. Koga, A.M. Jorge Jr., S. Savoie, R. Schulz, and C.S. Kiminami, Microstructural Investigation of Fe-Cr-Nb-B Amorphous/Nanocrystalline Coating Produced by HVOF, *Mater. Design*, 2016, **111**(1), p 608–615. <https://doi.org/10.1016/j.matdes.2016.09.027>
13. J. Cheng et al., Microstructure and Fracture Toughness of the FePSiB-Based Amorphous/Nanocrystalline Coatings, *Mat. Sci. Eng. A-Struct.*, 2017, **696**(1), p 341–347. <https://doi.org/10.1016/j.msea.2017.04.082>
14. Y. Zhou et al., Microstructures and Tribological Properties of Fe-Based Amorphous Metallic Coatings Deposited via Supersonic Plasma Spraying, *J. Therm. Spray Technol.*, 2017, **26**(6), p 1257–1267. <https://doi.org/10.1007/s11666-017-0582-1>
15. G.Y. Koga et al., Production and Corrosion Resistance of Thermally Sprayed Fe-Based Amorphous Coatings from Mechanically Milled Feedstock Powders, *Metall. Mater. Trans. A*, 2018, **49**(10), p 4860–4870. <https://doi.org/10.1007/s11661-018-4785-y>
16. J. Zhou et al., Novel In Situ Transformable Coating for Elevated-Temperature Applications, *J. Therm. Spray Technol.*, 2010, **19**(5), p 950–957. <https://doi.org/10.1007/s11666-010-9498-8>
17. V. Varadaraajan, R.K. Guduru and, P.S. Mohanty, Synthesis and Microstructural Evolution of Amorphous/Nanocrystalline Steel Coatings by Different Thermal-Spray Processes, *J. Therm. Spray Technol.*, 2013, **22**(4), p 452–462. <https://doi.org/10.1007/s11666-013-9885-z>
18. S.K. Nayak et al., Multi-Scale Mechanical Properties of Fe-Based Amorphous/Nanocrystalline Composite Coating Synthesized by HVOF Spraying, *J. Alloy. Compd.*, 2020, **825**, 154120. <https://doi.org/10.1016/j.jallcom.2020.154120>
19. A. Kumar et al., Fe-Based Amorphous/Nanocrystalline Composite Coating by Plasma Spraying: Effect of Heat Input on Morphology, Phase Evolution and Mechanical Properties, *J. Alloy. Compd.*, 2019, **771**(827e), p 837. <https://doi.org/10.1016/j.jallcom.2018.09.024>
20. H. Zhang et al., The Effect of High-Velocity Oxy-Fuel Spraying Parameters on Microstructure, Corrosion and Wear Resistance of Fe-Based Metallic Glass Coatings, *J. Non-Cryst. Solids*, 2014, **406**(1), p 37–44. <https://doi.org/10.1016/j.jnoncrsol.2014.09.041>
21. B. Huang et al., Wear and Corrosion Resistant Performance of Thermal-Sprayed Fe-Based Amorphous Coatings: A Review, *Surf. & Coat. Technol.*, 2019 <https://doi.org/10.1016/j.surfcoat.2019.124896>
22. Q. Yang et al., Compositional Dependence of Microstructure and Tribological Properties of Plasma Sprayed Fe-Based Metallic Glass Coatings, *Sci. China Technol. SC*, 2012, **55**(5), p 1335–1342. <https://doi.org/10.1007/s11431-012-4821-x>

Publisher's Note Springer Nature remains neutral with regard to jurisdictional claims in published maps and institutional affiliations.